REVIEW

Recent Progress in Large-Area Perovskite Photovoltaic Modules

Haifei Wang[1] · Zhixiao Qin[1] · Yanfeng Miao[1] · Yixin Zhao[1]

Abstract

Perovskite solar cells (PSCs) have undergone a dramatic increase in laboratory-scale efficiency to more than 25%, which is comparable to Si-based single-junction solar cell efficiency. However, the efficiency of PSCs drops from laboratory-scale to large-scale perovskite solar modules (PSMs) because of the poor quality of perovskite films, and the increased resistance of large-area PSMs obstructs practical PSC applications. An in-depth understanding of the fabricating processes is vital for precisely controlling the quality of large-area perovskite films, and a suitable structural design for PSMs plays an important role in minimizing energy loss. In this review, we discuss several solution-based deposition techniques for large-area perovskite films and the effects of operating conditions on the films. Furthermore, different structural designs for PSMs are presented, including the processing technologies and device architectures.

Keywords Perovskite solar cells · Perovskite solar modules · Large-scale perovskite films · Solution-based coating methods

Introduction

Perovskite material is considered as one of the most promising candidates for next-generation solar cells because of its excellent optoelectronic properties, such as a high optical absorption coefficient [1, 2], low exciton binding energy [3, 4], long carrier diffusion length [5, 6], high defect tolerance [7, 8], and low-cost fabrication [9–11]. Moreover, it has a changeable composition with a formula of ABX_3, where A generally represents a monovalent cation, such as a methylamine cation (MA^+), formamidine cation (FA^+), or Cs^+; B is Pb^{2+}, Sn^{2+}, or another divalent metal cation; and X is an iodine, bromine, or chlorine anion. Furthermore, perovskite structure can be regulated from three dimensions (3D) to lower dimensions [12, 13]. The changeable composite and dimension features endow an adjustable bandgap of ~1.2 eV to 3.0 eV [14–17] and can be applied in single-junction solar cells and tandem solar cells [18–22].

During the past decade, the power conversion efficiencies (PCEs) of perovskite solar cells (PSCs) at the laboratory scale (active area ≈ 0.1 cm^2) have increased from 3.8 to 25.7%, which is comparable with that of silicon solar cells [23–29]. However, most highly efficient PSCs are based on the spin-coating method, which is not suitable for large-scale fabrication because of its radial nonuniformity caused by centrifugal force [30, 31]. Therefore, the areas of perovskite solar modules (PSMs) prepared by the spin-coating method are usually less than 100 cm^2 [19, 32, 33]. Hence, scalable deposition technologies with high efficiency, excellent reproducibility, easy controllability, and low operating costs are key factors for practical PSMs. According to the areas of PSMs, PSMs can be classified as minimodule (< 200 cm^2), submodule (200–800 cm^2), small module (800–6500 cm^2), standard module (6500–14,000 cm^2), and large module (> 14,000 cm^2) [28, 34]. Various strategies have been developed to deposit large-area perovskite films with high quality, such as blade coating [35, 36], slot-die coating [37, 38], spray coating [39, 40], and inkjet printing [41]. The PSM efficiencies have increased to over 20%, and the module areas have increased from tens to hundreds of square centimeters [34, 42, 43] (Fig. 1a). For instance, Panasonic achieved a module efficiency of 17.9% with an aperture area of 804 cm^2 using the inkjet printing method [44]. Nonetheless, few standard or large modules have been reported, and most reported PSMs are under 100 cm^2 with a nearly 30%

✉ Yanfeng Miao
   yanfengmiao@sjtu.edu.cn

✉ Yixin Zhao
   yixin.zhao@sjtu.edu.cn

1   School of Environmental Science and Engineering, Frontiers Science Center for Transformative Molecules, Shanghai Jiao Tong University, Shanghai 200240, China

Fig. 1 **a** Top PCEs of PSMs in different years. The numbers in the brackets are the areas of modules and references, respectively, where aa, ap, and da denote the active area, aperture area, and designated area of PSMs, respectively. **b** Certified top PCEs of PSMs as a function of area. The data are from Refs. [34, 44, 70]
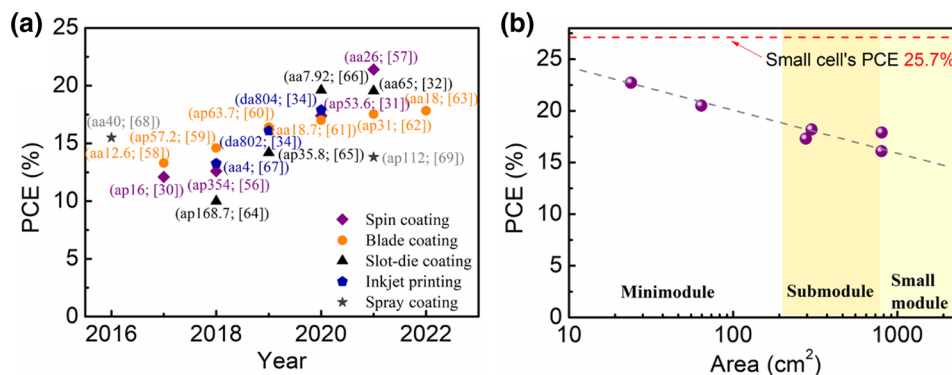
efficiency drop compared with small cells [25, 44, 45]. As exhibited in Fig. 1b, PCEs decrease quickly with increasing module areas.

PSMs have high requirements for the uniformity of the films because nanoscale phase impurities and lead iodide inclusions not only trap photogenerated charge carriers but also accelerate PSCs degradation [45–48]. A major challenge impeding PSCs application is how to fabricate high-quality, large-area perovskite films with eminent uniformity, high coverage, and low defect density. Recently, PSMs have undergone rapid development, and an understanding of their mechanism has been further developed. Some previous reviews related to large-area PSMs mainly focused on the modification methods for perovskite films [45, 49–51] and charge transport materials [52–55].

In this review, we focus on scalable solution-based deposition methods for perovskite films. We also discuss the designing process of PSMs and illustrate the operational factors. Finally, we summarize the challenges standing in the way of plant-scale applications and provide several future research directions for enhancing the PCE and stability of PSMs.

## Solution-Based Coating Methods for Large-Area Perovskite Films

In PSCs, the quality of the perovskite layer plays a decisive role in the efficiencies and stabilities of the final PSMs. Thus, in this section, we discuss the advantages and disadvantages of different fabrication methods for large-scale perovskite films.

Nucleation and Crystal Growth Mechanism

The general nucleation and grain growth process can be divided into three steps [71–75]. First, because of the continuous evaporation of the solvent, the precursor concentration increases to form a saturation solution (Cs). Because of the presence of a nucleation barrier, no nuclei are generated until the solution concentration is up to the critical concentration (Cc). Once the precursor concentration reaches Cc, many nuclei are generated quickly and begin to grow, and the number of nuclei increases rapidly until the concentration drops below Cc. Then, nuclei generation nearly stops while the grains continue to grow. When the concentration remains above Cc, the solutes are consumed mainly by the formation of new nuclei. Normally, this process is finished quickly. Next, when the solution concentration drops below Cc, the solutes are expended primarily by crystal growth. If the solvent evaporates at a low rate, only a few nuclei are generated, which results in coarse and porous films with large grains. In contrast, a high solvent evaporation rate leads to the formation of more nuclei. Therefore, controlling the evaporation rate of the solvent is vital for realizing high-quality perovskite films, and several methods have been developed to facilitate this process, such as gas flow [76], substrate/solution preheating [35], and vacuum flashing [77].

The nucleation rate is also limited by solution and substrate properties. Huang and coauthors [78] investigated the effects of wettability by depositing perovskite films on several types of hole transport layers (HTLs) with different wettabilities. They found that more nuclei were generated on the wettable HTLs, while large-aspect-ratio grain growth (2.3–7.9) was obtained on non-wetting HTLs because of the limited heterogeneous nucleation with larger nucleus spacing and enhanced migration of the grain boundary during grain growth caused by a smaller drag force. Pylnev et al. [79] explored the effects of substrate wettability on the nucleation and grain growth of perovskite by depositing perovskite films on a double-layered TiO_2/SnO_2 with different wettabilities. The changed wettability of the TiO_2/SnO_2 surface was obtained by hydrophobic recovery after UV treatment. They found that nucleation occurs more easily on a wettable surface, but only a 14% bigger grain size was observed when the contact angle increased from 3° to 72°.
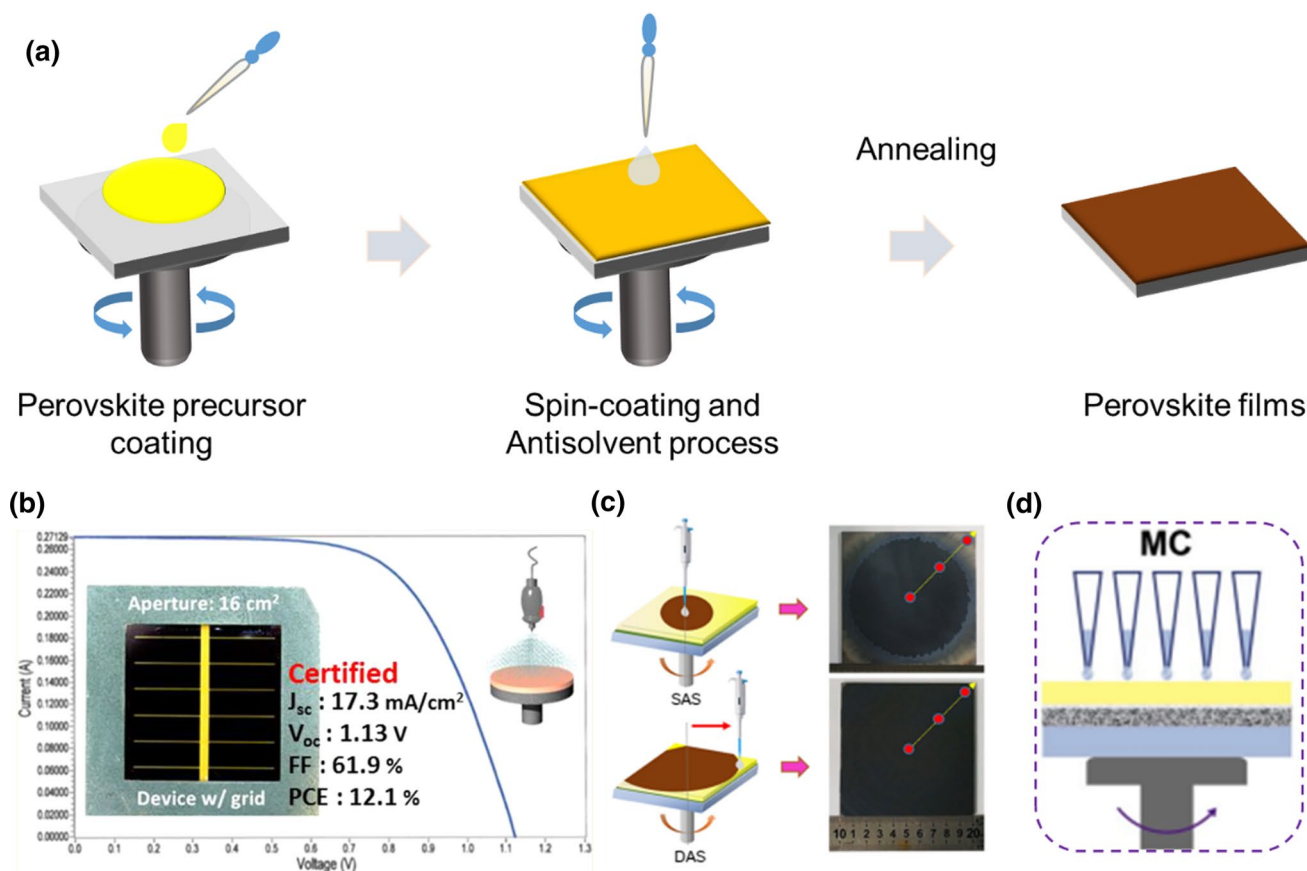
Fig. 2 **a** Schematic illustration of the spin-coating process involving antisolvent. **b** *J–V* curves of PSM prepared with antisolvent spray processing. The insets are the schematics of PSMs and spray antisolvent processing. Reproduced with permission from Ref. [30]. Copyright © 2017, American Chemical Society. **c** Schematic illustration of different antisolvent dropping methods of the commonly used static antisolvent (SAS) process (the top image) and dynamic antisolvent extracting (DAS) method (the bottom image). Reproduced with permission from Ref. [31]. Copyright © 2019, John Wiley and Sons. **d** Schematic illustration of the antisolvent process by multi-tip pipette. Reproduced with permission from Ref. [91]. Copyright © 2019, John Wiley and Sons

Spin Coating

Spin coating is the most commonly adopted method for depositing perovskite films in the laboratory because of its easy operation, low equipment cost, and eminent reproducibility. During the spin-coating process, the precursor solution is preloaded on the substrate center and is driven to spread over the entire surface of the substrate by centrifugal force while the excess precursor solution is expelled, as shown in Fig. 2a. The film thickness is determined by the rotating speed and the properties of the precursor solution, including the volatility and viscosity of the solvent, the temperature, and the initial solution concentration [80]. The film quality can be controlled by varying the solvents, the precursor compositions, the annealing temperature, the operational atmosphere, and particularly the humidity [80–84]. Moreover, the spinning speed has a great influence on the final film morphology by regulating the solvent evaporation rate [32]. In the past, introducing antisolvent has

helped the rapid development of PSCs in laboratory-scale and minimodules because using antisolvent changes the path from wet films to intermediate-phase films [83–88]. Notably, most of the highly efficient PSCs are fabricated involving the use of antisolvents [25, 26, 89]. Generally, quick solvent removal is needed to generate enough nuclei to form dense and uniform films [71–73]. Using antisolvent enables the quick extraction of solvent to reach the critical concentration and generate enough nuclei to form fully covered, dense intermediate films [85, 90].

However, getting homogeneous films on large-size substrates for the spin-coating method is difficult because of the increasing centrifugal force along the radial direction. In addition, to form homogeneous pinhole-free intermediate films, the antisolvent should be dropped quickly but softly at a certain time and then uniformly spread over the entire substrate. This process can be controlled at a small size, but it becomes difficult when the size of the substrate is enlarged.

To apply antisolvent in large-area substrates, different antisolvent processes have been developed. Kim et al. [30] performed this process by spraying antisolvent (the inset of Fig. 2b). With this method, the antisolvent could be simultaneously dropped on the entire surface of the substrate, and a certified PCE of 12.1% on an aperture area of 16 cm² was achieved (Fig. 2b). Huang and coauthors [31] changed the commonly used static antisolvent processing into dynamic processing (Fig. 2c) and achieved a PCE of 17.82% on the module's aperture area of 53.64 cm² with a short-circuit current of 101.4 mA and open-circuit voltage of 13.56 V. They further expanded the antisolvent processing by replacing the single-tip pipette with a multi-tip pipette (Fig. 2d), which enabled the antisolvent to be quickly and homogenously spread over the liquid perovskite films [91]. These methods exhibit advantages over traditional antisolvent quenching processing, but they are inapplicable when further enlarging the substrate.

The spin-coating method occupies a vital position in perovskite solar cell development because it provides an easy and effective approach for investigating the processing mechanisms of PSCs and minimodule PSMs. However, it is inappropriate to realize larger-area perovskite films with high uniformity and quality in submodules because of the radial, uneven centrifugal force. Many reports show PCEs of more than 20% on an active area of approximately 1 cm² [33, 89, 92], but few reports show a PCE of over 15% with an active area larger than 100 cm² [56, 93]. Carlo et al. [94] achieved efficiencies of 18.71% and 17.79% based on substrate sizes of 2.5×2.5 cm² and 10×10 cm² with active areas of 2.25 cm² and 48 cm², respectively, while only 11.9% was obtained when the substrate size increased to 20×20 cm² with an active area of 192 cm². More importantly, a substantial waste of precursor ink and a discontinuous fabrication feature further inhibit the large-scale application of the spin-coating method in PSMs.
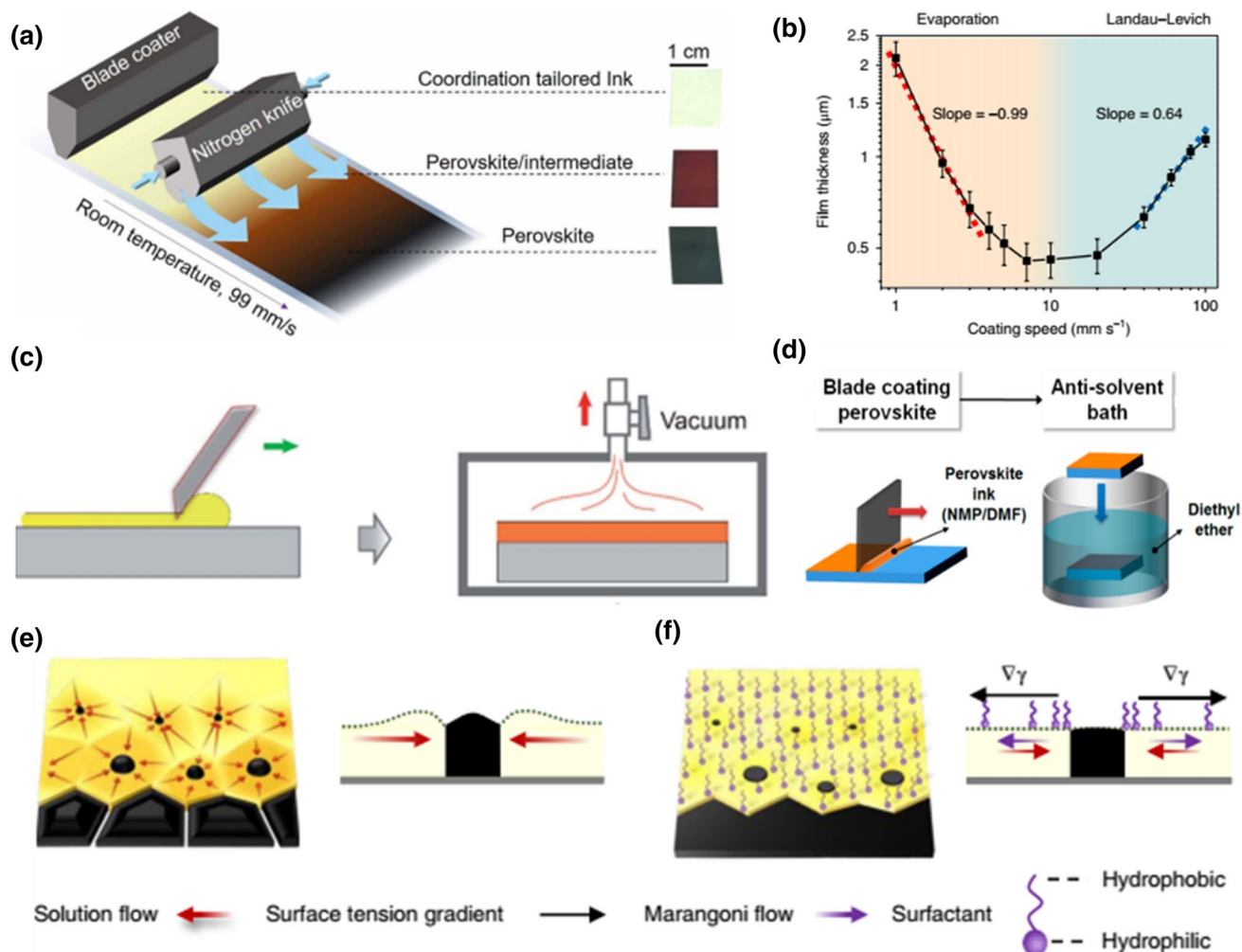
Blade Coating

According to the difference in blade coaters, blade coating can be divided into knife/doctor-blade coating and bar/rod coating [95, 96]. These techniques are close analogs and suitable for the roll-to-roll (R2R) manufacture of large-area perovskite films. Figure 3a presents a schematic illustration of the general blade coating process with the assistance of a gas knife to accelerate solvent volatilization. Similar to the spin-coating method, the coating solution is preloaded on the substrate, and a liquid film is formed by moving the blade coater or substrate.

According to the blade coating speed, the coating process can be divided into three cases: the evaporation regime (under a low coating rate), mixed regime (under a medium coating rate), and Landau–Levich regime (under a high coating rate), as shown in Fig. 3b [59, 97]. A transition between regimes can be triggered by changing the solution concentration, deposition temperature, and the distance between the substrate and blade. When the operating process is under a sufficiently low coating speed (related to the evaporation regime), solid films are directly obtained without forming liquid/wet films. The main characteristic of the evaporation regime is that the film thickness decreases with increasing coating speed. This characteristic results from the capillary flow toward the three-phase contact line, which is also called the coffee-ring effect [98, 99]. Moreover, the surface tension gradient induced by the ink concentration gradient may trigger Marangoni flow to enhance or repress the capillary flow [97, 98]. He et al. [100] demonstrated a feasible, meniscus-assisted solution printing method to deposit large-grained perovskite films with enhanced crystallization and high crystal orientation in the evaporation regime with a very low coating speed of 12 μm/s. Because of the fast solvent evaporation at the three-phase contact line of air, ink, and substrate, the deposition velocity equals the receding speed of the meniscus. This low coating speed enables the outward convective flow to just supplement the evaporated solvent and ceaselessly transport the perovskite precursors to the contact line, thus facilitating perovskite film deposition with micrometer-scale grains and preferred orientation. Overall, in the evaporation case, the final films are affected by complex microscale liquid flows and must be carefully considered if the coating speed is in this regime.

In contrast, increasing thickness with increasing coating speed is the main feature of the Landau–Levich regime [97]. In addition, the wet films are formed after coating because of the high printing speed. Thus, additional treatments, such as substrate heating [101, 102], gas quenching [62, 96, 103], vacuum flashing [104, 105], and antisolvent extraction [46], are usually needed to control the nucleation and grain growth processes. These techniques are also widely used in other upscaling deposition methods to facilitate the nucleation and grain growth processes during the wet film drying process. Zhong et al. [106] explored the effects of substrate temperature on MAPbI₃ film morphology through in situ optical and X-ray scattering techniques. They found that the operating temperature can mediate the polymorphism and composition of the solvates by changing the solvent evaporation rate. Low temperatures lead to different compositions and yield poor PCE. Elevated temperatures lead to directly crystallizing from the solgel ink without forming intermediate-phase films, which results in large and compact domains of perovskite accompanied by enhanced PCE [106, 107].

Figure 3c, d shows that vacuum-assisted drying and antisolvent bathing processes are not synchronized with wet film formation. Because of the narrow time window for the post-treatments, determining the best time is difficult, resulting in poor-quality perovskite films with pinholes or rough surfaces

Fig. 3 **a** Schematic of the general blade coating process assisted by gas quenching. Reproduced with permission from Ref. [60]. Copyright © 2019, AAAS. **b** Perovskite film thickness as a function of the printing rate. Reproduced with permission from Ref. [59]. Copyright © 2018, Springer Nature. **c** Schematic illustration of vacuum flashing-assisted blade coating. Reproduced with permission from Ref. [104]. Copyright © 2018, Royal Society of Chemistry. **d** Schematic illustration of antisolvent bathing-assisted blade coating. Reproduced with permission from Ref. [46]. Copyright © 2018, American Chemical Society. **e** Schematic diagram of the directional microscale liquid flow toward the perovskite islands during wet film drying. Reproduced with permission from Ref. [59]. Copyright © 2018, Springer Nature. **f** Schematic illustration of restrained ink flow in the presence of a surfactant. $\nabla\gamma$ represents the surface tension gradient. Reproduced with permission from Ref. [59]. Copyright © 2018, Springer Nature

[58, 107]. To solve this problem, Zhu and coauthors [58] demonstrated that the methylammonium chloride (MACl) additive coupled with solvent adjusting (NMP:DMF) can effectively endow a wider precursor-processing window of up to ~8 min. Using the antisolvent bathing-assisted blade coating method, they achieved an average efficiency of 17.33% on an area of 1.2 cm^2 and a PCE of 13.3% for 12.6 cm^2 PSMs. Additionally, many studies show that mixed solvents are beneficial for widening the precursor-processing window [40, 58, 108]. For the mixed solvents, a component with a low boiling point, such as DMF and ACN, serves as the main solvent, while another solvent usually exhibits a high Gutmann's donor number (D_N) (with strong coordinating ability) and relatively low volatility. These cosolvents include dimethyl sulfoxide (DMSO), dimethylacetamide, dimethylpropyleneurea, and N-methyl-2-pyrrolidone (NMP). The main solvent favors nucleation and growth by quickly evaporating, while the cosolvent can stabilize the precursor ink (widen the processing window) by strong interaction with the Pb^{2+} center. Very recently, Qi and coauthors [109] revealed that N-methyl-2-pyrrolidone can impede the formation of the perovskite-DMF complex intermediates that lead to poor film quality. Combining the introduction of MACl, they achieved an efficiency of 15.3% on a module area of 205 cm^2. Additionally, more works on
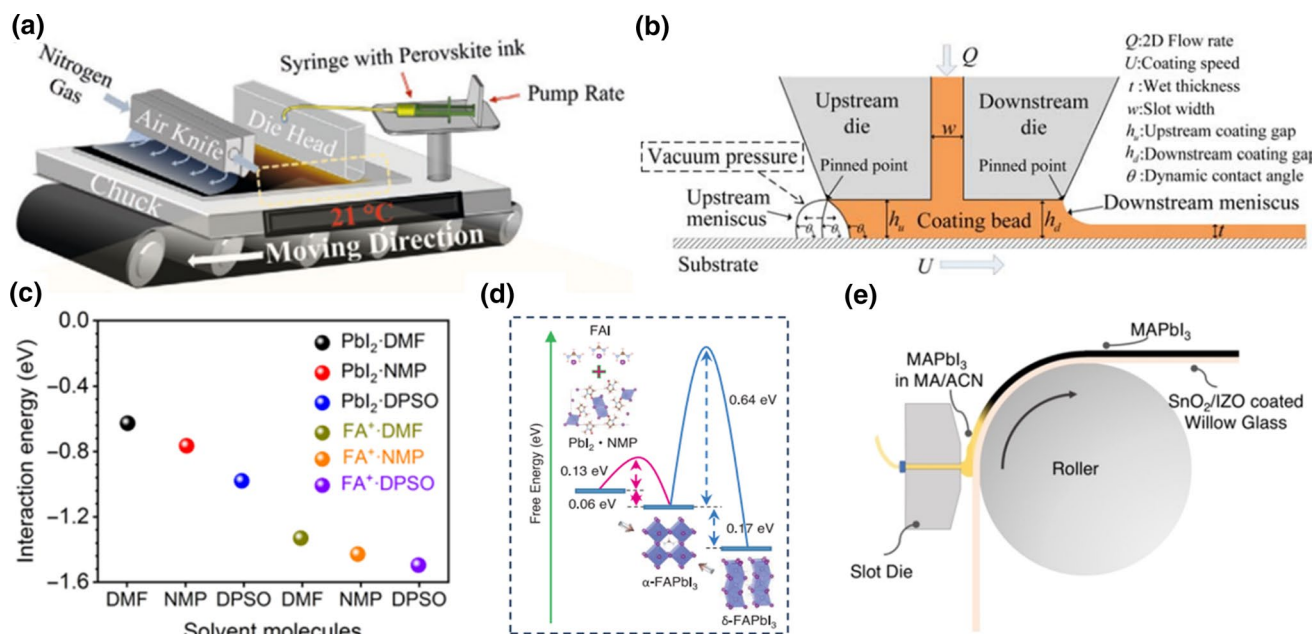
Fig. 4 a Schematic of slot-die coating assisted with an air knife. Reproduced with permission from Ref. [114]. Copyright © 2021, John Wiley and Sons. b Schematic illustration of a capillary coating bead during the slot-die coating process. Reproduced with permission from Ref. [113]. Copyright © 2021, John Wiley and Sons. c Calculated interaction energy of DMF, NMP, or DPSO molecules with FA+ and PbI$_2$ species. Reproduced with permission from Ref. [122].

Copyright © 2021, AAAS. d DFT calculated the free energy of the formation of α-phase FAPbI$_3$ perovskites from PbI$_2$·NMP + FAI or δ-FAPbI$_3$. Reproduced with permission from Ref. [32]. Copyright © 2021, AAAS. e Schematic diagram of the slot-die coating process on a flexible substrate with an R2R coater. Reproduced with permission from Ref. [124]. Copyright © 2018, American Chemical Society

additives and cosolvents are provided in the previous reports [110, 111].

In addition to controlling solvent evaporation, regulating the microscale ink flow dynamics is also an effective way to control the nucleation and grain growth during the wet film drying process [112]. Huang and coauthors [59] reported a method for controlling the fluid drying dynamics by introducing a surfactant of L-α-phosphatidylcholine (LP). They found that during the drying process of wet perovskite films, once the grain islands are generated, the microscale fluid flows (labeled as red arrows in Fig. 3e) transport the perovskite solutes to the islands, which results in rough and porous perovskite films. The microscale liquid flows are speculated to result from a faster evaporation rate of solvent around the islands. As shown in Fig. 3f, after LP is introduced, the solution flows lead to the accumulation of LP molecules on the periphery of the perovskite islands. Additionally, a reduced surface tension gradient from the body ink to the island is established because of the increasing LP concentration. This surface tension gradient can induce the Marangoni flow to restrain the solution flow. Furthermore, adding LP can improve the adhesion of the precursor solution to the non-wetting surface by diminishing the surface tension of the precursor ink. Thus, the uniform dense perovskite films were fabricated using the blade coating method with a high

coating rate of up to 180 m/h. Based on these perovskite films, the PSMs achieved efficiencies of 15.3% and 14.6% for aperture areas of 33.0 cm^2 and 57.2 cm^2, respectively. More interestingly, this method can also be used in other solution-based deposition techniques that use the liquid drying process.

Blade coating is a simple and R2R-compatible technology with the features of low operating cost and a facile controlling process. It is a promising method for upscaling the manufacture of perovskite films. However, many operating conditions need to be optimized for dense, pinhole-free, and uniform perovskite films. The optimization processes include the basic operating parameters and wet film solidification control, as illustrated above.

Slot-Die Coating

Slot-die coating is a versatile technique that is widely used to deposit thin films with high uniformity. Benefiting from its pre-metered feature, the thickness of wet films can be preset and precisely adjusted by optimizing the ink flow rate and the substrate moving speed or coating speed [113]. Figure 4a shows that a slot-die coater generally consists of an ink-supplying system and a die head [114]. Moreover, to precisely control the crystallization process, an air knife

and substrate heating system are usually introduced. During operation, precursor ink is continuously supplied from the ink reservoir to the die head by a pump, which endows slot-die coating with the feature of large-scale, continuous manufacturing with high reproducibility. Once the precursor ink reaches the substrate, a capillary coating bead is formed to link the die head and the substrate through two edges, which are referred to as upstream and downstream menisci (Fig. 4b). Additionally, the shape of the coating bead plays an important role in the thickness and morphology of the final films [45]. While the die head or substrate moves relatively, a uniform wet thin film is generated by dragging the capillary coating bead. To obtain high-quality perovskite films, some operating parameters should be carefully designed, such as the ink flow rate, coating speed, coating gap, and operating temperature [113, 115–117]. In addition, the properties of precursor ink, including the concentration and composition of solutions, the solvent volatility, and the surface tension of the coating ink, play a decisive role in the quality of the final films by intervening in the solidification process of the wet films. Furthermore, similar to the blade coating technique, various additional treatments, such as gas quenching, vacuum drying, and antisolvent bathing, can be used to control the nucleation and grain growth during the drying process of liquid films [116, 118].

Liu and coauthors [66] explored the effects of N_2 pressure on PSC efficiency. They found that high-pressure nitrogen extraction (HPNE) can accelerate solvent volatilization and decrease the ink temperature, which helps to achieve a widened processing window in a well-designed coating process. They demonstrated that HPNE leads to yellow-phase intermediate perovskite film, which is prone to forming large-area, high-quality perovskite films after annealing. Further combining the surface passivation with tetramethylammonium tetrafluoroborate ([M_4N]BF_4), the final PCE efficiency is up to 19.6% with an active area of 7.92 cm^2. Fievez et al. [116] reached a similar conclusion that a higher gas flow rate leads to higher substrate coverage. They further demonstrated that reducing the distance between the gas knife and the substrate is beneficial for forming a more homogeneous lateral gas flow. Cotella et al. [119] found that substrate preheating and a cold air knife could induce an increasing temperature gradient from the surface to the bottom of the wet film. The relatively high substrate temperature could facilitate the drying dynamics and nucleation process, while the thermal gradient favored vertical crystal growth [119, 120]. Thus, the final perovskite films exhibited an improved surface coverage and vertical orientation feature.

In addition to directly controlling solvent evaporation, antisolvent processing and vacuum flashing are also employed [108, 118, 121]. Similar to blade coating, the processing window must be widened by an additive or cosolvent to enhance the operating efficiency. For instance, diphenyl sulfoxide (DPSO), a Lewis base additive with nonvolatility and high D_N, is used to improve the nucleation barrier through strong interaction with the solute in the precursor inks (Fig. 4c) [122]. Combined with the post-antisolvent bathing extraction processing, the related solar module (active area of 20.77 cm^2) achieved a certified quasi-stabilized PCE of 16.63%. Notably, the encapsulated PSMs retained 95% of the initial PCE after continuous illumination of 1-sun equivalent white light for 1187 h at the maximum power point.

In addition, the nucleation and grain growth processes can be modulated by the solvents or intermediate phase. Li et al. [114] revealed that using pure 2-methoxy-ethanol (2-ME) as the solvent leads to porous films while adding DMSO to 2-methoxy-ethanol can dramatically modify the morphology of MAPbI$_3$ film. The in situ X-ray diffraction and small-angle X-ray scattering results show that a certain amount of DMSO can impede the generation of an adverse intermediate product (MAPbI$_3$-2-ME) and facilitate the generation of a MAPbI$_3$ perovskite phase. Huang and coauthors revealed that N-methyl-2-pyrrolidone (NMP) can convert the intermediate phase of FA$_2$Pb$_3$I$_8$·4DMF and δ-(FACs)PbI$_3$ into lead halide–NMP adducts (PbI$_2$·NMP and PbX$_2$·NMP/DMF complexes) when DMF is used as the solvent [32]. The lead halide–NMP adducts can directly convert into α-phase perovskite by in situ reacting with embedded CsI/FAI at low temperature with a lower free energy requirement (Fig. 4d), which sidesteps the formation of a δ-phase perovskite. Combined with excess PbCl$_2$ additive, large-area, dense, and uniform perovskite films were prepared based on the slot-die coating technique. The final PSMs realized high efficiency of 20.42% (certified efficiency of 19.3%) with an active area of 17.1 cm^2, and an efficiency of 19.54% was achieved when the active area increased to 65.0 cm^2.

Most importantly, slot-die coating is a promising technique for the R2R upscaling fabrication of PSCs [123]. As presented in Fig. 4e, using a high initial concentration and a volatile solvent (MA/ACN), Dou et al. [124] demonstrated a partial R2R slot-die coating on a flexible substrate in an ambient environment and achieved an efficiency of 14.1%. More importantly, they found that 98% of relative crystallinity could be accomplished at room temperature.

Inkjet Printing

Inkjet printing is an all-around technology for controllable and large-scale deposition of thin films from a colloidal dispersion or homogeneous solution inks [49, 125, 126]. In contrast to the blade coating and slot-die coating techniques, inkjet printing is a noncontact printing method, and the ink can be deposited on a flexible or rigid substrate with a smooth, rough, or even curved surface. In the basic mechanism of the inkjet printing technique, the ink is misted
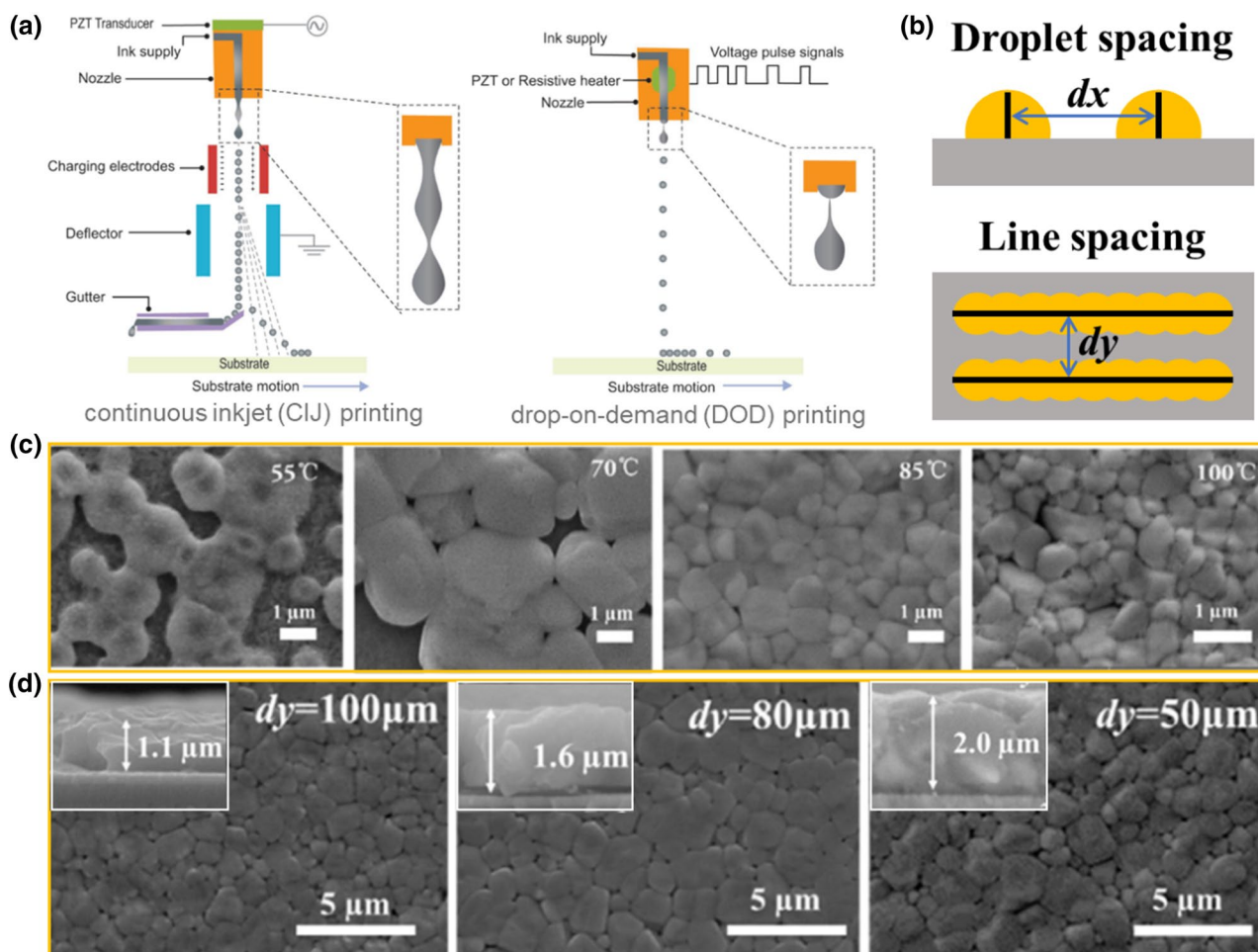
Fig. 5 **a** Schematic illustration of inkjet coating. Reproduced with permission from Ref. [125]. Copyright © 2017, John Wiley and Sons. **b** Schematic illustration of the droplet spacing (d_x, the top image) and the line spacing (d_y, the bottom image) in the inkjet coating process. **c** Top-view SEM images of the perovskite films printed under different operating temperatures. Reproduced with permission from Ref. [130]. Copyright © 2021, John Wiley and Sons. **d** Top-view SEM images of the perovskite films printed with different line spacings (d_y); the insets are cross-sectional SEM images. Reproduced with permission from Ref. [130]. Copyright © 2021, John Wiley and Sons

into small droplets and ejected out through a fine nozzle onto the substrate to form predesigned patterns. According to different droplet supplying methods, the inkjet printing techniques can be divided into two modes: continuous inkjet (CIJ) printing and drop-on-demand (DOD) inkjet printing [125]. Figure 5a shows schematic diagrams of the different inkjet printing methods. For CIJ printing, continuous ink droplets are generated and partially deposited on the substrate, which results in less use of ink. In contrast, DOD inkjet printing can generate a single droplet at once when required; thus, much higher ink usage is achieved compared to continuous inkjet printing. The ejection of ink droplets is realized through a regular pressure pulse, which is produced by the explosion of thermally induced bubbles or the mechanical distortion of a piezoelectric transducer. Thus, DOD inkjet printing can be divided into two modes: thermal and piezoelectric. When a regular pressure pulse is used,

the printing ink is expelled from the nozzles to generate a single droplet, and then the droplet is accurately settled on the designed location by moving the printer head or the substrate. Inkjet printing is a digitally controlled technique that endows high reproducibility and high throughput. In addition, the droplet size and droplet distance (Fig. 5b) also have a great influence on the morphology and thickness of the final films [127, 128].

Gao et al. [129] found that a low concentration and printing speed could lead to poor surface morphology. Additionally, porous perovskite film is obtained when printing at low temperatures. By optimizing the operating parameters of ink concentration, printing speed, and substrate temperature, they achieved a PCE of 16.78% on an effective area of 120 cm^2. Yang et al. [130] reported a similar result that low operating temperature leads to a discontinuous morphology with low coverage (Fig. 5c), which results from a low
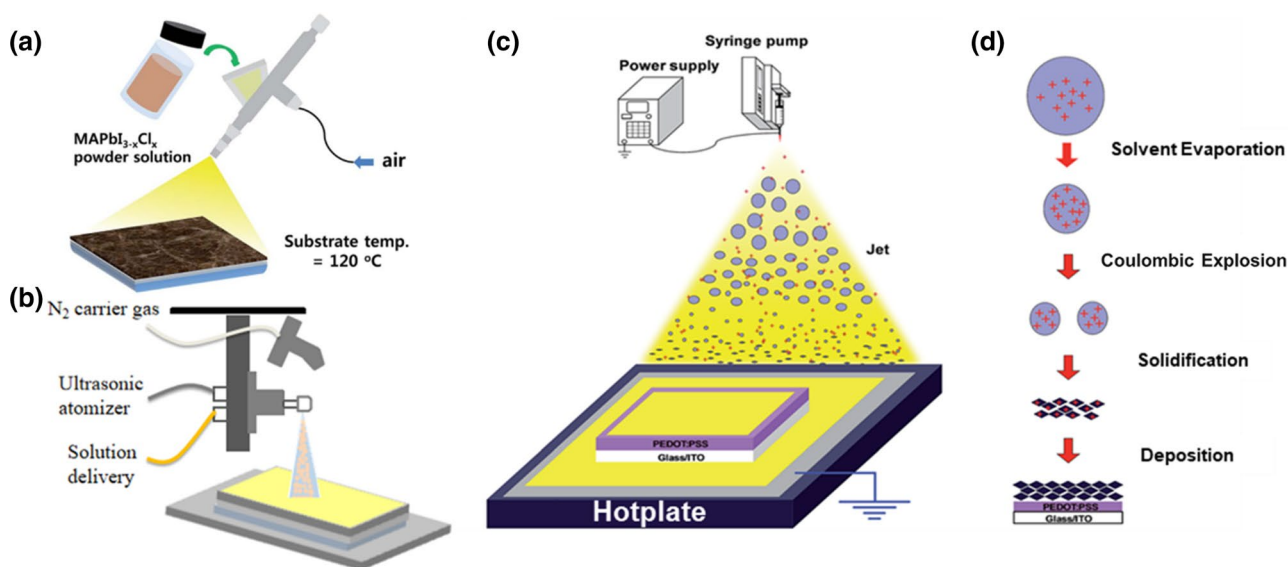
Fig. 6 **a** Schematic illustration of pneumatic spray coating. Reproduced with permission from Ref. [68]. Copyright © 2016, Royal Society of Chemistry. **b** Schematic illustration of ultrasonic spray coating. Reproduced with permission from Ref. [135]. Copyright © 2020, American Chemical Society. **c** Electrospray coating and **d** a schematic of solidified crystal formation by electrospray coating. Reproduced with permission from Ref. [138]. Copyright © 2017, Royal Society of Chemistry

nucleation rate and long grain growth time. By increasing the temperature to 85 °C, dense perovskite film with relatively small crystal grains was obtained. They further demonstrated that the line space can affect not only the thickness but also the surface morphology of perovskite films (Fig. 5d). Optimizing the line space could gain a smooth film with vertically grown perovskite grains.

In addition, when printing with a high boiling point solvent at low temperature, only the wet films are obtained. Thus, subsequent treatments, such as vacuum-assisted drying, are required to prevent inhomogeneous grain growth caused by the coffee-ring effect [41, 128, 131]. For example, Mathies et al. [132] demonstrated that directly annealing the wet film leads to a rough surface morphology with large perovskite islands, while the films become smooth and fully covered when a vacuum is used. Liang et al. [67] reported that vacuum-assisted thermal annealing can facilitate intermediate-phase formation by fast removal of solvent, which benefits fabricating a uniform, dense perovskite film with a large area.

Inkjet printing is a promising method for upscaling PSC fabrication. Its advantages include a contact-free and digital controlling process, high reproducibility, and high printing efficiency. However, various operating limits should be determined by the experimental design of features such as ink properties, printing temperature, printing speed, drying conditions, droplet size, and droplet and line spaces. Furthermore, the print heads are less durable and prone to being blocked by the precipitate caused by the drying of the precursor ink.

Spray Coating

Similar to inkjet printing, spray coating is also a noncontact printing technology. Thus, it is suitable for depositing thin films on a substrate with a smooth, rough, or even curved surface. However, the misted droplets for spray coating are uncontrollably deposited on the substrate, while this process is precisely set for inkjet printing. According to the differences in atomization mechanisms, spray coating can be mainly divided into three categories: pneumatic spray coating, ultrasonic spray coating, and electrospray coating [133]. For pneumatic spray coating, compressed gas, such as air, N_2, or Ar, is used to atomize and disperse the precursor ink to form aerosol [134]. Then, the atomized ink is driven onto the substrate by gravity and the compressed gas, as presented in Fig. 6a. The main advantage is a very low operating cost with simple equipment. Although the size of a mist droplet can be controlled by the gas pressure and flow rate, generating monodisperse droplets is a challenge. Moreover, the high-pressure gas with strong flow used to atomize the ink may cause large material losses. As for ultrasonic spray coating, the coating inks are misted by the mechanical vibrations produced by the ultrasonic waves used, and then the atomized inks are delivered onto the target surface by adding a low-pressure carrier gas as well as using gravity, as shown in Fig. 6b [135]. The droplets generated by ultrasonic vibrations are ultrafine (usually at micrometer size) and uniform [136]. Additionally, the size of a mist droplet can be adjusted by changing the resonant frequency and ink flow rate. Generally, a higher ultrasonic frequency leads to

a smaller droplet size. Furthermore, the low-pressure carrier gas flow produces negligible splashing; thus, the utilization rate of precursor ink can be greatly enhanced. In contrast to the above two methods, the atomic process is achieved by electrostatic repulsion in electrospray coating. Figure 6c, d presents the electrospray coating process and high-voltage electric field-assisted atomizing process, respectively. During the coating processing, the ink is supplied through a designed metallic capillary, which is charged with static electricity to several thousand volts (Fig. 6c) [137]. Then, because of the shrinkage caused by solvent evaporation, the increasing Coulombic repulsion leads to an explosion of ejected coating ink into mists with narrow size distributions. Furthermore, this process can realize a wide and continuous adjusting of the droplet dimensions from the nanoscale to the microscale, as shown in Fig. 6d [133, 136, 138]. The generated ultrafine ink mists are attracted to the target substrate surface that is fixed on a grounded stage. In addition, nearly all of the mists are deposited on the designed surface by electrostatic attraction. Therefore, the ink use is further improved compared to ultrasonic spray coating.

During the spray coating process, once the ink leaves the spray nozzle, solvent evaporation occurs, and the solution concentration begins to increase. If the solution concentration increases to the critical concentration before reaching the substrate, nuclei will generate, which leads to poor-quality film with pinholes and a rough surface [136, 139, 140]. A critical concentration should be formed immediately when the droplets reach the substrate so that the substrate surface can serve as a nucleation center [139, 141]. Therefore, the flight time must be suitable for depositing uniform, dense perovskite films, and it is affected simultaneously by droplet size, the gas flow rate, the gap between the substrate and spraying nozzle, operating temperature, and ink properties.

Hong et al. [137] investigated the effects of droplet size on the morphology and crystallinity of the final perovskite films, as well as the performance of the prepared device. The results show that if the droplet size is too small, solvent evaporation will be too quick to form smooth and pinhole-free perovskite films, while an oversized droplet leads to the coffee-ring effect. Barrows et al. [39] explored the effects of substrate temperature on the morphologies of the final perovskite films. They found that a low operating temperature leads to large grains but low surface coverage due to a low solvent removal rate with few nuclei. Therefore, some post-treatments, such as hot casting [137, 142], vacuum-assisted drying [40, 143], and antisolvent bath quenching [144, 145], are also needed to facilitate nucleation and grain growth during the solidification process of liquid/wet films.

Furthermore, spray coating is the preferred method for graded structure films with a composition gradient. A composition gradient can be achieved by changing the coating inks layer by layer. For instance, Heo et al. [69] prepared

$CsPbI_{3-x}Br_x$ composition gradient films by successively depositing a $CsPbI_2Br$ layer and a $CsPbI_3$ layer. They found that this graded structure can enhance light absorption and benefit charge carrier separation and collection by inducing the redistribution of the electrical field. The graded $CsPbI_{3-x}Br_x$-based PSMs achieved a PCE of 13.82% with an aperture area of 112 cm^2.

Structural Design of Perovskite Solar Modules

Classification of Perovskite Solar Modules

In contrast to a small solar cell, PSMs comprise many subcells. To describe the module efficiency more conveniently and clearly, module areas are usually divided into a designated illumination area, aperture area, and total area, as illustrated in Fig. 7a [146, 147]. The designated illumination area presents the region where light illuminates when measuring the module performance. The aperture area includes the entire subcell area and interconnection area of the module. The total area is the sum of the total projected area, including the frame area. Moreover, the active areas, which exhibit photoactivity during performance measurement, are usually used to estimate PSM performance.

For large-area PSCs, the charge carriers must be transported a long distance in a transparent conducting electrode with relatively low conductivity. This requirement inevitably results in additional resistance loss [148, 149]. This energy loss can be diminished by module designing and shortening the charge carrier transmission path. According to different connection modes between subcells, the PSMs can be divided into parallel and series modules [94, 150].

PSMs in Parallel Connection

For parallel-connected PSMs, a major feature is that the current is the sum of subcell currents. This feature is preferable in tandem solar cells because the adjustable current can benefit from matching with the current of the bottom cells [30, 151]. Figure 7b presents a type of parallel-connected PSM. In this kind of module, two scribes, commonly named P1 and P2, are used to achieve the final design. P1 removes the transparent conductive oxide (TCO) layer and isolates the connection between the final top electrode and the bottom electrode. P2 is operated after depositing the perovskite layer, electron transport layer (ETL), and HTL but before depositing the metal electrode. P2 makes space for metal grid deposition on the bottom electrode. For an ideal P2, the materials deposited on TCO are removed completely, while the TCO layer remains undamaged. These scribe procedures can be avoided when metal grids are predeposited
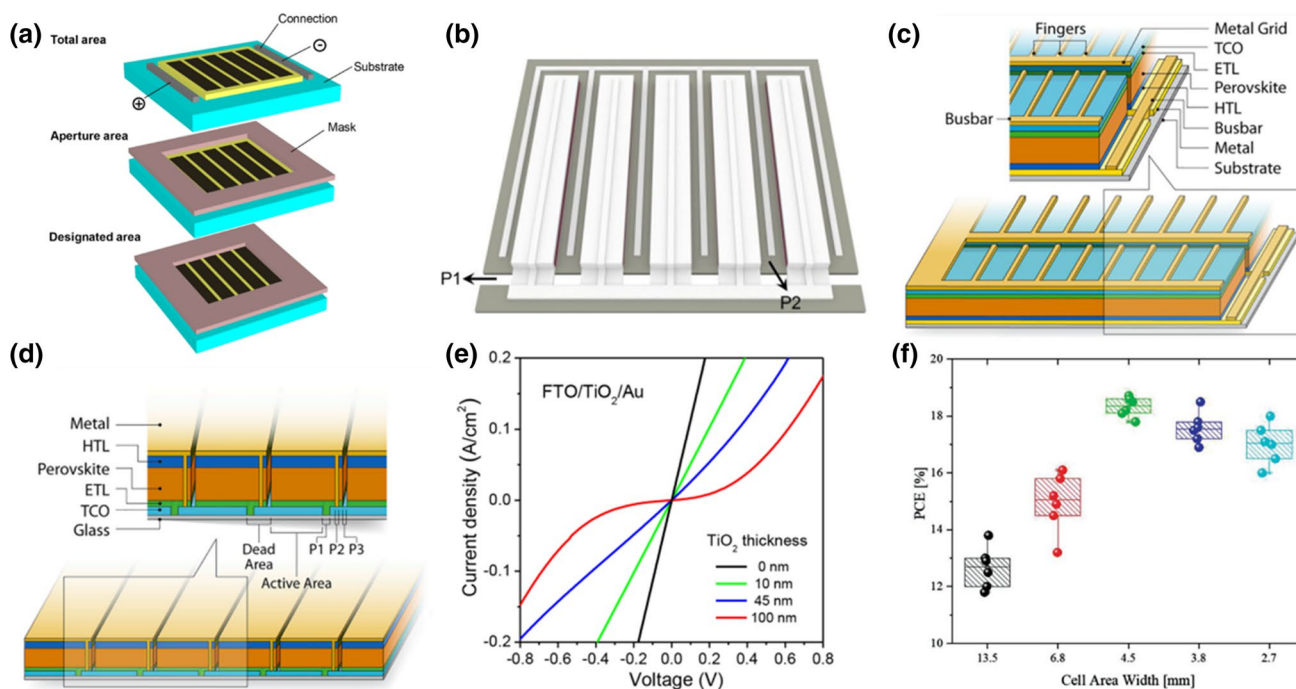
Fig. 7 **a** Schematic of defined areas for PSM performance measurement. Reproduced with permission from Ref. [162]. Copyright © 2018, American Chemical Society. **b** Schematic of parallel PSMs with P1 and P2 scribes. Reproduced with permission from Ref. [122]. Copyright © 2021, AAAS. **c** Schematic of parallel PSMs with grid interconnect. Reproduced with permission from Ref. [163]. Copyright © 2021, John Wiley and Sons. **d** Schematic of series PSMs interconnected by P1, P2, and P3 scribes. Reproduced with permission from Ref. [163]. Copyright © 2021, John Wiley and Sons. **e** J–V curve of FTO/TiO$_2$/Au with different TiO$_2$ thicknesses. Reproduced with permission from Ref. [46]. Copyright © 2018, American Chemical Society. **f** PSM performances with different cell area widths. Reproduced with permission from Ref. [94]. Copyright © 2022, John Wiley and Sons

on the TCO or used directly as bottom metal electrodes with transparent top electrodes, as shown in Fig. 7c [151–153]. Metal grids (consisting of fingers and a busbar) are used to collect the current from the subcells to decrease the charge transport distance in TCO. However, many more metals or conductors are in demand to reduce the resistive loss caused by the high current, and a balance between lessening resistive losses and increasing the grid-shadowed areas must be struck. Moreover, high-quality and uniform perovskite films with high reproducibility are difficult to manufacture using a solution procedure on metal substrates or substrates loaded with metal grids.

PSMs in Series Connection

The series PSMs comprise a range of parallel subcells, as shown in Fig. 7d. Each subcell is connected by the design of three parallel scribes referred as P1, P2, and P3. This process is also called the "monolithic interconnection" method. P1 scribe is used to remove the conductive layer (TCO or other conductors) on the substrate to divide the large substrate into a series of small, parallel patterns. These patterns are insulated from each other by P1 scribes, and each pattern corresponds to a subcell. After the depositions of HTL, the perovskite layer, and ETL, the P2 scribe is operated near P1. The ideal P2 clears the deposited materials without damaging the TCO layer (the magnified image in Fig. 7d). The residual TiO$_2$ and damages in the TCO layer are adverse to PSM performance [154]. Zhu and coauthors [46] explored the effects of residual TiO$_2$ on contact resistance. As presented in Fig. 7e, residual TiO$_2$ induces a change of the interconnection contact type between the metal electrode and TCO from Ohmic contact to a Schottky diode behavior. The P3 scribe is operated to isolate the top electrode with adjacent cells to form the final series of PSMs.

The output voltage is the accumulated voltage of each subcell, while the value of the current equals the value of the smallest subcell's current. A limited current flow can efficiently diminish the parasitic loss caused by the relatively low TCO conductivity [155]. However, because of the direct contact of perovskite and the metal electrode at the P2 scribe region, the chemical reactions between perovskite and the

metal electrode have an important impact on PSM stability [65, 122, 156]. Qi and coauthors [156] demonstrated that air could facilitate the reaction between methylammonium lead perovskite and silver electrodes, and this reaction could be limited in a dry nitrogen atmosphere.

Subcell Design in PSMs

As for PSMs, the connection regions (scribe areas or metal grid-covered areas) are inactive and are called a "dead area," as exhibited in Fig. 7c, d. To estimate this dead area, the geometric fill factor (GFF) is introduced, which is the ratio of active areas and aperture areas (the sum of active areas and dead areas) of PSMs. To increase the GFF, the connection area should be decreased as much as possible.

The scribing process can be performed by laser ablation or mechanical scribing. Laser ablation can achieve a high GFF of over 95% with high reproducibility [91, 94, 152, 157]. However, the damage to perovskite film caused by the residual heat effect near the ablation line is difficult to avoid, particularly during P2 ablation. The operating limitations for laser ablation, such as the laser wavelength, output power, pulse frequency, and duration, must be carefully determined to minimize the damage to perovskite and perform etching [151, 152, 158]. Compared with laser ablation, mechanical scribing may be a potential method because of its low operating cost and negligible damage to perovskite. However, operating on a flexible substrate and gaining a high GFF are challenging [46, 69, 159].

Moreover, for certain aperture areas, the number of subcells also affects efficiency and stability [94]. When increasing the subcell number, a shorter distance is needed for charge carriers to reach the electrodes, which helps minimize the resistive loss. However, in this case, more contact lines inevitably lead to a lower GFF. More scribe lines may also aggravate the damage to the perovskite, leading to poor stability and performance. In contrast, a large subcell size can realize a high GFF while increasing the current flow through each subcell, resulting in a higher resistance-related loss [151, 154]. A trade-off between resistive loss and the GFF should be made, and the power losses related to the dead area (f_d) and the TCO resistance (f_{TCO}) can be illustrated by the loss factor (f) [160, 161]:

$$f = f_d + f_{TCO}$$
$$= \frac{W_d}{W_d + W_a} + \frac{1}{3} \cdot R_{sh} \frac{J_{mpp}}{V_{mpp}} \cdot \frac{W_a^3}{W_d + W_a} \quad (1)$$

where W_d and W_a are the width of the dead area and active area, respectively; R_{sh} is the TCO sheet resistance; V_{mpp} and J_{mpp} present the voltage and current density at the maximum power point, respectively. For certain values of W_a, the

power losses can be minimized by decreasing the dead area width [161]. For a definite dead area width, the total power losses will decrease first and then increase with the width of the active area. The subsequent increase in power losses results in increased TCO resistance-induced energy loss. These calculated results are consistent with experiments (Fig. 7f) [94]. The best PEC was achieved with a cell area width of 4.5 mm when the GFF was 91%.

Stability of PSMs

Some previous reports have summarized the stability of PSCs/PSMs under different conditions and the strategies for stabilizing them [164–168]. Therefore, we will mainly focus on the stability challenge caused by the interconnections of subcells in PSMs. The interconnection region exhibits a faster degradation during the aging process, which is mainly caused by the direct contact of perovskite and the metal electrode at the P2 scribe and the exposure of perovskite to the environment at the P3 scribe [165, 169]. Chen and coauthors [170] found that a compact and chemically inert Bi layer between the HTL layer and metal electrode can serve as a permeation barrier that simultaneously protects the perovskite from moisture and the metal electrode from iodine corrosion. Bi interlayer-based devices presented greatly enhanced stability and maintained 88% of their initial PCE after aging for over 6000 h in ambient air. Combining the ALD–Al_2O_3 thin-film encapsulation, no obvious color change was observed for the as-prepared PSMs after soaking in water for several minutes [122]. The encapsulated modules retained 97% of their initial PCE after 10 000 h under day/night cycling. Aside from Bi, Cr can also serve as a barrier layer to prevent chemical reactions between perovskite and the metal electrode [171]. Han and coauthors [65] demonstrated that the chemical reaction between perovskite and the electrode could be limited by building low-dimensional diffusion barriers (DBLs). The DBLs comprised thermally and chemically stable materials, such as metal oxide nanoparticles (0D), inert silicon-based organic polymers (1D), and 2D inorganic materials. More importantly, the device performance could be enhanced by the DBLs by passivating the surface defect of perovskite. Using graphitic carbon nitride (g-C_3N_4) as DBLs, they achieved a PCE of 15% on a module area of 36 cm^2, and the device retained over 95% of its initial PCE after heating at 85 °C for 1000 h. The promising strategy of superseding a noble metal electrode with inert and inexpensive materials without a great PCE drop, such as carbon materials, can not only avoid the electrode–perovskite reaction but also further reduce cost [172–174].

Summary and Perspective

In summary, small PSCs exhibit excellent PCE of over 25%, which is comparable to that of silicon solar cells. However, high efficiencies are achieved based on the spin-coating method, and a dramatic efficiency drop is observed for large-area PSMs. Although many mature upscaling deposition technologies have been successfully introduced to solve this problem, more efforts need to be focused on the fabrication process of large-area perovskite films to obtain further in-depth understanding, particularly of the effects of solvent properties, such as volatility, surface tension, and coordination ability, precursors (additives and chemical compositions), and the operating parameters of depositing technology, on the nucleation and grain growth processes. At the same time, technologies need to be developed to minimize the power loss caused by PSM structural design. In particular, the contact resistance between the metal electrodes and TCO electrodes should be reduced by carefully designing the preparation process. In addition, highly efficient and inexpensive charge extraction materials should be developed to replace the expensive materials, such as [6,6]-phenyl C61-butyric acid methyl ester (PCBM) and 2,2′,7,7′-tetrakis-(N,N-di-p-methoxyphenyl-amine)-9,9′-spirobifluorene (spiro-MeOTAD), because this tactic has great potential for reducing the precursor cost of industrial manufacture. In addition to the efficiency, the stability of PSMs under humidity, UV light, heat, and oxygen is of equal importance for large-scale practical applications. Although recent studies performed the device stability test over thousands of hours, this duration is far from meeting the requirement for large-scale applications with a lifetime of over 10 years. As the first protecting barrier, encapsulation plays a crucial role in PSC stability in moisture and oxygen. Encapsulation can also prevent toxic lead from entering the environment and is conducive to raw material recycling. Finally, developing lightweight and high-performance, flexible PSMs is a great advantage compared to conventional silicon solar cells because of the soft crystal and size-tunable properties of perovskite [175, 176].

Declarations

Conflict of interest The authors declare that they have no conflict of interest.

References

1. Zhao YX, Zhu K (2016) Organic–-inorganic hybrid lead halide perovskites for optoelectronic and electronic applications. Chem Soc Rev 45(3):655–689. https://doi.org/10.1039/C4CS00458B

2. Zuo CT, Bolink HJ, Han HW et al (2016) Advances in perovskite solar cells. Adv Sci (Weinh) 3(7):1500324

3. Galkowski K, Mitioglu A, Miyata A et al (2016) Determination of the exciton binding energy and effective masses for methylammonium and formamidinium lead tri-halide perovskite semiconductors. Energy Environ Sci 9(3):962–970. https://doi.org/10.1039/C5EE03435C

4. Miyata A, Mitioglu A, Plochocka P et al (2015) Direct measurement of the exciton binding energy and effective masses for charge carriers in organic–inorganic tri-halide perovskites. Nat Phys 11(7):582–587

5. Zhao YX, Zhu K (2013) Charge transport and recombination in perovskite $(CH_3NH_3)PbI_3$ sensitized TiO_2 solar cells. J Phys Chem Lett 4(17):2880–2884. https://doi.org/10.1021/JZ401527Q

6. Stranks SD, Eperon GE, Grancini G et al (2013) Electron-hole diffusion lengths exceeding 1 micrometer in an organometal tri-halide perovskite absorber. Science 342(6156):341–344

7. Chu WB, Zheng QJ, Prezhdo OV et al (2020) Low-frequency lattice phonons in halide perovskites explain high defect tolerance toward electron-hole recombination. Sci Adv 6(7):eaaw7453

8. Steirer KX, Schulz P, Teeter G et al (2016) Defect tolerance in methylammonium lead triiodide perovskite. ACS Energy Lett 1(2):360–366

9. Yusoff AR, Nazeeruddin MK (2016) Organohalide lead perovskites for photovoltaic applications. J Phys Chem Lett 7:851–866. https://doi.org/10.1039/C4EE00942H

10. Chen HN, Wei ZH, Zheng XL et al (2015) A scalable electrodeposition route to the low-cost, versatile and controllable fabrication of perovskite solar cells. Nano Energy 15:216–226. https://doi.org/10.1016/j.nanoen.2015.04.025

11. Li ZQ, Zhao YZ, Wang X et al (2018) Cost analysis of perovskite tandem photovoltaics. Joule 2(8):1559–1572. https://doi.org/10.1016/j.joule.2018.05.001

12. Han CX, Wang Y, Yuan JB et al (2022) Tailoring phase alignment and interfaces via polyelectrolyte anchoring enables large-area 2D perovskite solar cells. Angew Chem Int Ed Engl 61(36):e202205111

13. Swarnkar A, Marshall AR, Sanehira EM et al (2016) Quantum dot-induced phase stabilization of α-$CsPbI_3$ perovskite for high-efficiency photovoltaics. Science 354(6308):92–95

14. Sutton RJ, Eperon GE, Miranda L et al (2016) Bandgap-tunable cesium lead halide perovskites with high thermal stability for

efficient solar cells. Adv Energy Mater 6(8):1502458. https://doi.org/10.1002/aenm.201502458

15. Wang R, Huang TY, Xue JJ et al (2021) Prospects for metal halide perovskite-based tandem solar cells. Nat Photon 15(6):411–425

16. Noh JH, Im SH, Heo JH et al (2013) Chemical management for colorful, efficient, and stable inorganic-organic hybrid nanostructured solar cells. Nano Lett 13(4):1764–1769

17. Sun HX, Tian W, Wang XF et al (2020) In situ formed gradient bandgap-tunable perovskite for ultrahigh-speed color/spectrum-sensitive photodetectors via electron-donor control. Adv Mater 32(14):e1908108

18. Rajagopal A, Yang Z, Jo SB et al (2017) Highly efficient perovskite-perovskite tandem solar cells reaching 80% of the theoretical limit in photovoltage. Adv Mater 29(34):1702140

19. Xiao K, Lin RX, Han QL et al (2020) All-perovskite tandem solar cells with 24.2% certified efficiency and area over 1 cm^2 using surface-anchoring zwitterionic antioxidant. Nat Energy 5(11):870–880

20. Gota F, Langenhorst M, Schmager R et al (2020) Energy yield advantages of three-terminal perovskite-silicon tandem photovoltaics. Joule 4(11):2387–2403. https://doi.org/10.1016/j.joule.2020.08.021

21. Chen X, Jia ZY, Chen Z et al (2020) Efficient and reproducible monolithic perovskite/organic tandem solar cells with low-loss interconnecting layers. Joule 4(7):1594–1606. https://doi.org/10.1016/j.joule.2020.06.006

22. Wang CL, Zhao Y, Ma TS et al (2022) A universal close-space annealing strategy towards high-quality perovskite absorbers enabling efficient all-perovskite tandem solar cells. Nat Energy 7(8):744–753

23. Kojima A, Teshima K, Shirai Y et al (2009) Organometal halide perovskites as visible-light sensitizers for photovoltaic cells. Am Chem Soc 131(17):6050–6051

24. Lee MM, Teuscher J, Miyasaka T et al (2012) Efficient hybrid solar cells based on meso-superstructured organometal halide perovskites. Science 338(6107):643–647

25. Minjin K, Jaeki J, Lu HZ et al (2022) Conformal quantum dot-SnO2 layers as electron transporters for efficient perovskite solar cells. Science 375(6578):302–306

26. Li Z, Li B, Wu X et al (2022) Organometallic-functionalized interfaces for highly efficient inverted perovskite solar cells. Science 376(6591):416–420. https://doi.org/10.1126/science.abm85661

27. Min H, Lee DY, Kim J et al (2021) Perovskite solar cells with atomically coherent interlayers on SnO2 electrodes. Nature 598(7881):444–450

28. Green MA, Dunlop ED, Hohl-Ebinger J et al (2021) Solar cell efficiency tables (version 59). Prog Photovolt Res Appl 30:3–12

29. Zhao Y, Ma F, Qu ZH et al (2022) Inactive (PbI$_2$)$_2$RbCl stabilizes perovskite films for efficient solar cells. Science 377(6605):531–534

30. Kim J, Yun JS, Cho Y et al (2017) Overcoming the challenges of large-area high-efficiency perovskite solar cells. ACS Energy Lett 2(9):1978–1984. https://doi.org/10.1021/acsenergylett.7b00573

31. Bu TL, Liu XP, Li J et al (2019) Dynamic anti-solvent engineering for spin -coating of 10 ×10 cm2 perovskite solar module approaching 18%. Solar RRL 4(2):1900263. https://doi.org/10.1002/solr.201900263

32. Bu TL, Li J, Li HY et al (2021) Lead halide-templated crystallization of methylamine-free perovskite for efficient photovoltaic modules. Science 372(6548):1327–1332

33. Fang ZH, Wang LY, Mu XJ et al (2021) Grain boundary engineering with self-assembled porphyrin supramolecules for highly efficient large-area perovskite photovoltaics. J Am Chem Soc 143(45):18989–18996. https://doi.org/10.1021/jacs.1c07518

34. Champion Photovoltaic Module Efficiency Chart. NREL. https://www.nrel.gov/pv/module-efficiency.html. Accessed 28 July 2022. https://www.nrel.gov/pv/module-efficiency.html

35. Deng YH, Peng E, Shao YC et al (2015) Scalable fabrication of efficient organolead trihalide perovskite solar cells with doctor-bladed active layers. Energy Environ Sci 8(5):1544–1550. https://doi.org/10.1039/C4EE03907F

36. Vesce L, Stefanelli M, Herterich JP et al (2021) Ambient air blade-coating fabrication of stable triple-cation perovskite solar modules by green solvent quenching. Sol RRL 5(8):2100073. https://doi.org/10.1002/solr.202100073

37. Bernard S, Jutteau S, Mejaouri S et al (2021) One-step step slot-die coating deposition of wide-bandgap perovskite absorber for highly efficient solar cells. Sol RRL 5:2100391

38. Le TS, Saranin D, Gostishchev P et al (2021) All-slot-die-coated inverted perovskite solar cells in ambient conditions with chlorine additives. Sol RRL 6(2):2100807. https://doi.org/10.1002/solr.202100807

39. Barrows AT, Pearson AJ, Kwak CK et al (2014) Efficient planar heterojunction mixed-halide perovskite solar cells deposited via spray-deposition. Energy Environ Sci 7(9):2944–2950. https://doi.org/10.1039/C4EE01546K

40. Bishop JE, Smith JA, Greenland C et al (2018) High-efficiency spray-coated perovskite solar cells utilizing vacuum-assisted solution processing. ACS Appl Mater Interfaces 10(46):39428–39434

41. Li SG, Jiang KJ, Su MJ et al (2015) Inkjet printing of CH3NH3PbI3 on a mesoscopic TiO$_2$ film for highly efficient perovskite solar cells. J Mater Chem A 3(17):9092–9097. https://doi.org/10.1039/C4TA05675B

42. Matteocci F, Razza S, Di Giacomo F et al (2014) Solid-state solar modules based on mesoscopic organometal halide perovskite: A route towards the up-scaling process. Phys Chem Chem Phys 16(9):3918–3923. https://doi.org/10.1039/C3CP55313B

43. Shen WZ, Zhao YX, Liu F (2022) Highlights of mainstream solar cell efficiencies in 2021. Front Energy 16(1):1–8. https://doi.org/10.1007/s11708-022-0816-x

44. Green M, Dunlop E, Hohl-Ebinger J et al (2021) Solar cell efficiency tables (version 58). Prog Photovolt Res Appl 29:657–667

45. Lee D-K, Park N-G (2021) Materials and methods for high-efficiency perovskite solar modules. Sol RRL 6(3):2100455

46. Yang MJ, Kim DH, Klein TR et al (2018) Highly efficient perovskite solar modules by scalable fabrication and interconnection optimization. ACS Energy Lett 3(2):322–328

47. MacPherson S, Doherty TAS, Winchester AJ et al (2022) Local nanoscale phase impurities are degradation sites in halide perovskites. Nature 607(7918):294–300

48. Tan S, Yavuz I, Weber MH et al (2020) Shallow iodine defects accelerate the degradation of α-phase formamidinium perovskite. Joule 4(11):2426–2442

49. Yang CQ, Zhi R, Uller Rothmann M et al (2021) Toward commercialization of efficient and stable perovskite solar modules. Sol RRL 6(3):2100600

50. Choi K, Choi H, Min J et al (2019) A short review on interface engineering ofperovskite solar cells: a self-assembled monolayer and its roles. Sol RRL 4(2):1900251

51. Mahapatra A, Prochowicz D, Tavakoli MM et al (2020) A review of aspects of additive engineering in perovskite solar cells. J Mater Chem A 8(1):27–54

52. Valadi K, Gharibi S, Taheri-Ledari R et al (2021) Metal oxide electron transport materials for perovskite solar cells: A review. Environ Chem Lett 19(3):2185–2207

53. Mahmood K, Sarwar S, Mehran MT (2017) Current status of electron transport layers in perovskite solar cells: materials and properties. RSC Adv 7(28):17044–17062

54. Reza KM, Mabrouk S, Qiao Q (2018) A review on tailoring PEDOT: PSS layer for improved performance of perovskite solar cells. Proc Nat Res Soc 2:02004

55. Chen YC, Meng Q, Zhang LR et al (2019) SnO2-based electron transporting layer materials for perovskite solar cells: a review of recent progress. J Energy Chem 35:144–167

56. Higuchi H, Negami T (2018) Largest highly efficient 203 × 203 mm2 CH3NH3PbI3 perovskite solar modules. J Appl Phys 57(8S3):08RE11

57. Liu C, Yang Y, Rakstys K et al (2021) Tuning structural isomers of phenylenediammonium to afford efficient and stable perovskite solar cells and modules. Nat Commun 12:6394

58. Yang MJ, Li Z, Reese MO et al (2017) Perovskite ink with wide processing window for scalable high-efficiency solar cells. Nat Energy 2:17038

59. Deng YH, Zheng XP, Bai Y et al (2018) Surfactant-controlled ink drying enables high-speed deposition of perovskite films for efficient photovoltaic modules. Nat Energy 3(7):560–566

60. Deng YH, Van Brackle CH, Dai XZ et al (2019) Tailoring solvent coordination for high-speed, room-temperature blading of perovskite photovoltaic films. Sci Adv 5(12):eaax7537

61. Lim KS, Lee DK, Lee JW et al (2020) 17% efficient perovskite solar mini-module via hexamethylphosphoramide (HMPA)-adduct-based large-area D-bar coating. J Mater Chem A 8(18):9345–9354

62. Yoo JW, Jang J, Kim U et al (2021) Efficient perovskite solar mini-modules fabricated via bar-coating using 2-methoxyethanol-based formamidinium lead tri-iodide precursor solution. Joule 5(9):2420–2436

63. He R, Nie S, Huang X et al (2021) Scalable preparation of high-performance ZnO–SnO2 cascaded electron transport layer for efficient perovskite solar modules. Sol RRL 6:2100639

64. di Giacomo F, Shanmugam S, Fledderus H et al (2018) Up-scalable sheet-to-sheet production of high efficiency perovskite module and solar cells on 6-in. substrate using slot Die coating. Sol Energy Mater Sol Cells 181:53–59

65. Bi EB, Tang WT, Chen H et al (2019) Efficient perovskite solar cell modules with high stability enabled by iodide diffusion barriers. Joule 3(11):2748–2760

66. Du MY, Zhu XJ, Wang LK et al (2020) High-pressure nitrogen-extraction and effective passivation to attain highest large-area perovskite solar module efficiency. Adv Mater 32(47):e2004979

67. Liang C, Li PW, Gu H et al (2018) One-step inkjet printed perovskite in air for efficient light harvesting. Sol RRL 2(2):1700217

68. Heo JH, Lee MH, Jang MH et al (2016) Highly efficient CH3NH3PbI3−xClx mixed halide perovskite solar cells prepared by re-dissolution and crystal grain growth via spray coating. J Mater Chem A 4(45):17636–17642

69. Heo JH, Zhang F, Xiao CX et al (2021) Efficient and stable graded CsPbI3−xBrx perovskite solar cells and submodules by orthogonal processable spray coating. Joule 5(2):481–494

70. Ding Y, Ding B, Kanda H et al (2022) Single-crystalline TiO2 nanoparticles for stable and efficient perovskite modules. Nat Nanotechnol 17(6):598–605

71. Ding B, Li Y, Huang SY et al (2017) Material nucleation/growth competition tuning towards highly reproducible planar perovskite solar cells with efficiency exceeding 20%. J Mater Chem A 5(15):6840–6848

72. Zhou YY, Game OS, Pang SP et al (2015) Microstructures of organometal trihalide perovskites for solar cells: their evolution from solutions and characterization. J Phys Chem Lett 6(23):4827–4839

73. Whitehead CB, Özkar S, Finke RG (2019) LaMer's 1950 model for particle formation of instantaneous nucleation and diffusion-controlled growth: A historical look at the model's origins, assumptions, equations, and underlying sulfur Sol formation kinetics data. Chem Mater 31(18):7116–7132

74. Lee JW, Lee DK, Jeong DN et al (2018) Control of crystal growth toward scalable fabrication of perovskite solar cells. Adv Funct Mater 29(47):1807047

75. Kwon SG, Hyeon T (2011) Formation mechanisms of uniform nanocrystals via hot-injection and heat-up methods. Small 7:2685–2702

76. Huang FZ, Dkhissi Y, Huang WC et al (2014) Gas-assisted preparation of lead iodide perovskite films consisting of a monolayer of single crystalline grains for high efficiency planar solar cells. Nano Energy 10:10–18

77. Li X, Bi DQ, Yi CY et al (2016) A vacuum flash-assisted solution process for high-efficiency large-area perovskite solar cells. Science 353(6294):58–62

78. Bi C, Wang Q, Shao YC et al (2015) Non-wetting surface-driven high-aspect-ratio crystalline grain growth for efficient hybrid perovskite solar cells. Nat Commun 6:7747

79. Pylnev M, Barbisan AM, Wei TC (2021) Effect of wettability of substrate on metal halide perovskite growth. Appl Surf Sci 541:148559. https://doi.org/10.1016/j.apsusc.2020.148559

80. Wang PY, Zhang XW, Zhou YQ et al (2018) Solvent-controlled growth of inorganic perovskite films in dry environment for efficient and stable solar cells. Nat Commun 9:2225

81. Dualeh A, Tétreault N, Moehl T et al (2014) Effect of annealing temperature on film morphology of organic-inorganic hybrid perovskite solid-state solar cells. Adv Funct Mater 24(21):3250–3258. https://doi.org/10.1002/adfm.201304022

82. Zhang TY, Xu QL, Xu F et al (2019) Spontaneous low-temperature crystallization of α-FAPbI3 for highly efficient perovskite solar cells. Sci Bull 64(21):1608–1616

83. Gu EEN, Tang XXF, Langner S et al (2020) Robot-based high-throughput screening of antisolvents for lead halide perovskites. Joule 4(8):1806–1822

84. Jeon NJ, Noh JH, Kim YC et al (2014) Solvent engineering for high-performance inorganic–organic hybrid perovskite solar cells. Nat Mater 13(9):897–903

85. Taylor AD, Sun Q, Goetz KP et al (2021) A general approach to high-efficiency perovskite solar cells by any antisolvent. Nat Commun 12:1878

86. Xiao MD, Huang FZ, Huang WC et al (2014) A fast deposition-crystallization procedure for highly efficient lead iodide perovskite thin-film solar cells. Angew Chem Int Ed Engl 53:9898–9903

87. Ghosh S, Mishra S, Singh T (2020) Antisolvents in perovskite solar cells: importance, issues, and alternatives. Adv Mater Interfaces 7(18):2000950

88. Tavakoli M, Yadav P, Prochowicz D et al (2019) Controllable perovskite crystallization via antisolvent technique using chloride additives for highly efficient planar perovskite solar cells. Adv Energy Mater 9(17):1803587

89. Li NX, Niu XX, Li L et al (2021) Liquid medium annealing for fabricating durable perovskite solar cells with improved reproducibility. Science 373(6554):561–567

90. Wei N, Chen Y, Wang X et al (2021) Multi-level passivation of MAPbI3 perovskite for efficient and stable photovoltaics. Adv Funct Mater 32:2108944

91. Wang C, Tan GY, Luo XP et al (2020) How to fabricate efficient perovskite solar mini-modules in lab. J Power Sources 466:228321

92. Peng J, Kremer F, Walter D et al (2022) Centimetre-scale perovskite solar cells with fill factors of more than 86 per cent. Nature 601(7894):573–578

93. Qiu LB, He SS, Ono LK et al (2019) Scalable fabrication of metal halide perovskite solar cells and modules. ACS Energy Lett 4(9):2147–2167

94. Angelo CL, Mahmoud Z, Narges YN et al (2022) Reducing losses in perovskite large area solar technology: laser design optimization for highly efficient modules and minipanels. Adv Energy Mater 12:2103420

95. Shim E (2010) Coating and laminating processes and techniques for textiles. Woodhead Publishing, Sawston

96. Lee DK, Jeong DN, Ahn TK et al (2019) Precursor engineering for a large-area perovskite solar cell with >19% efficiency. ACS Energy Lett 4(10):2393–2401

97. Le Berre M, Chen Y, Baigl D (2009) From convective assembly to Landau-Levich deposition of multilayered phospholipid films of controlled thickness. Langmuir 25(5):2554–2557

98. Tadmor R (2009) Marangoni flow revisited. J Colloid Interface Sci 332(2):451–454

99. Gu XD, Shaw L, Gu K et al (2018) The meniscus-guided deposition of semiconducting polymers. Nat Commun 9:534

100. He M, Li B, Cui X et al (2017) Meniscus-assisted solution printing of large-grained perovskite films for high-efficiency solar cells. Nat Commun 8:16045

101. Dai XZ, Deng Y, Van Brackle CH et al (2019) Scalable fabrication of efficient perovskite solar modules on flexible glass substrates. Adv Energy Mater 10(1):1903108

102. Deng YH, Dong QF, Bi C et al (2016) Air-stable, efficient mixed-cation perovskite solar cells with Cu electrode by scalable fabrication of active layer. Adv Energy Mater 6(11):1600372

103. Deng YH, Xu S, Chen SS et al (2021) Defect compensation in formamidinium–caesium perovskites for highly efficient solar mini-modules with improved photostability. Nat Energy 6:633–641

104. Xu ZY, Chen RH, Wu YZ et al (2019) Br-containing alkyl ammonium salt- enabled scalable fabrication of high-quality perovskite films for efficient and stable perovskite modules. J Mater Chem A 7(47):26849–26857

105. Zhang JW, Bu TL, Li J et al (2020) Two-step sequential blade-coating of high quality perovskite layers for efficient solar cells and modules. J Mater Chem A 8(17):8447–8454

106. Zhong YF, Munir R, Li JB et al (2018) Blade-coated organolead triiodide perovskite solar cells with efficiency >17%: an in situ investigation. ACS Energy Lett 3(5):1078–1085

107. Li JB, Munir R, Fan YY et al (2018) Phase transition control for high-performance blade-coated perovskite solar cells. Joule 2(7):1313–1330

108. Whitaker JB, Kim DH, Larson BW et al (2018) Scalable slot-Die coating of high performance perovskite solar cells. Sustain Energy Fuels 2(11):2442–2449

109. Bu TL, Ono LK, Li J et al (2022) Modulating crystal growth of formamidinium–caesium perovskites for over 200 cm^2 photovoltaic sub-modules. Nat Energy 7(6):528–536

110. Hamill JC Jr, Schwartz J, Loo YL (2018) Influence of solvent coordination on hybrid organic-inorganic perovskite formation. ACS Energy Lett 3(1):92–97

111. Lee JW, Kim HS, Park NG (2016) Lewis acid-base adduct approach for high efficiency perovskite solar cells. Acc Chem Res 49(2):311–319

112. Fan BJ, Xiong J, Zhang YY et al (2022) A bionic interface to suppress the coffee-ring effect for reliable and flexible perovskite modules with a near-90% yield rate. Adv Mater 34(29):e2201840

113. Ding XY, Liu JH, Harris TAL (2016) A review of the operating limits in slot Die coating processes. AIChE J 62(7):2508–2524

114. Li JJZ, Dagar J, Shargaieva O et al (2021) 20.8% slot-Die coated MAPbI3 perovskite solar cells by optimal DMSO-content and age of 2-ME based precursor inks. Adv Energy Mater 11:2003460

115. Huang SH, Guan CK, Lee PH et al (2020) Perovskite solar cells: toward all slot-Die fabricated high efficiency large area perovskite solar cell using rapid near infrared heating in ambient air (adv. energy mater 37/2020). Adv Energy Mater 10(37):2070155. https://doi.org/10.1002/aenm.202070155

116. Fievez M, Singh Rana PJ, Koh TM et al (2021) Slot-Die coated methylammonium-free perovskite solar cells with 18% efficiency. Sol Energy Mater Sol Cells 230:111189. https://doi.org/10.1016/j.solmat.2021.111189

117. Vak D, Hwang K, Faulks A et al (2015) Solar cells: 3D printer based slot-Die coater as a lab-to-fab translation tool for solution-processed solar cells (adv. energy mater. 4/2015). Adv Energy Mater 5(4):1401539. https://doi.org/10.1002/aenm.201401539

118. Zimmermann I, Al Atem M, Fournier O et al (2021) Sequentially slot-Die-coated perovskite for efficient and scalable solar cells. Adv Mater Interfaces 8:2100743

119. Cotella G, Baker J, Worsley D et al (2017) One-step deposition by slot-Die coating of mixed lead halide perovskite for photovoltaic applications. Sol Energy Mater Sol Cells 159:362–369. https://doi.org/10.1016/j.solmat.2016.09.013

120. Zhang TY, Chen YT, Kan M et al (2021) MA cation-induced diffusional growth of low-bandgap FA-Cs perovskites driven by natural gradient annealing. Research (Wash D C) 2021:9765106

121. Du MY, Zhao S, Duan LJ et al (2022) Surface redox engineering of vacuum-deposited NiO$_x$ for top-performance perovskite solar cells and modules. Joule 6(8):1931–1943. https://doi.org/10.1016/j.joule.2022.06.026

122. Yang ZC, Zhang WJ, Wu SH et al (2021) Slot-Die coating large-area formamidinium-cesium perovskite film for efficient and stable parallel solar module. Sci Adv 7(18):eabg3749

123. Hwang K, Jung YS, Heo YJ et al (2015) Toward large scale roll-to-roll production of fully printed perovskite solar cells. Adv Mater 27(7):1241–1247

124. Dou B, Whitaker JB, Bruening K et al (2018) Roll-to-roll printing of perovskite solar cells. ACS Energy Lett 3:2558–2565

125. Peng XJ, Yuan J, Shen S et al (2017) Solar cells: perovskite and organic solar cells fabricated by inkjet printing: progress and prospects. Adv Funct Mater 27(41):1703704

126. Wei ZH, Chen HN, Yan KY et al (2014) Inkjet printing and instant chemical transformation of a CH$_3$NH$_3$PbI$_3$/nanocarbon electrode and interface for planar perovskite solar cells. Angew Chem Int Ed Engl 53(48):13239–13243

127. Schackmar F, Eggers H, Frericks M et al (2020) Perovskite solar cells with all-inkjet-printed absorber and charge transport layers. Adv Mater Technol 6:2000271

128. Eggers H, Schackmar F, Abzieher T et al (2019) Inkjet-printed micrometer-thick perovskite solar cells with large columnar grains. Adv Energy Mater 10:1903184

129. Gao BW, Meng J (2021) Flexible CH$_3$NH$_3$PbI$_3$ perovskite solar cells with high stability based on all inkjet printing. Sol Energy 230:598–604. https://doi.org/10.1016/j.solener.2021.10.072

130. Zhang LH, Chen S, Wang XZ et al (2021) Ambient inkjet-printed high-efficiency perovskite solar cells: manipulating the spreading and crystallization behaviors of picoliter perovskite droplets. Sol RRL 5:2100106

131. Deegan (2000) Pattern formation in drying drops. Phys Rev E Stat Phys Plasmas Fluids Relat Interdiscip Topics 61(1):475–485

132. Mathies F, Abzieher T, Hochstuhl A et al (2016) Multipass inkjet printed planar methylammonium lead iodide perovskite solar cells. J Mater Chem A 4(48):19207–19213

133. Chou LH, Chan JMW, Liu CL (2022) Progress in spray-coated perovskite films for solar cell applications. Sol RRL 6(4):2101035

134. Shao YY, Zhang CY, Wang S et al (2019) Insight into the interfacial elastic contact in stacking perovskite solar cells. Adv Mater Interfaces 6(7):1900157

135. Cai HK, Liang XJ, Ye XF et al (2020) High efficiency over 20% of perovskite solar cells by spray coating via a simple process. ACS Appl Energy Mater 3(10):9696–9702

136. Kavadiya S, Niedzwiedzki DM, Huang S et al (2017) Electrospray-assisted fabrication of moisture-resistant and highly stable perovskite solar cells at ambient conditions. Adv Energy Mater 7(18):1700210

137. Hong SC, Lee G, Ha K et al (2017) Precise morphology control and continuous fabrication of perovskite solar cells using droplet-controllable electrospray coating system. ACS Appl Mater Interfaces 9:7879–7884

138. Lin PY, Chen YY, Guo TF et al (2017) Electrospray technique in fabricating perovskite-based hybrid solar cells under ambient conditions. RSC Adv 7(18):10985–10991

139. Chen HB, Ding XH, Pan X et al (2018) Comprehensive studies of air-brush spray deposition used in fabricating high-efficiency CH3NH3PbI3 perovskite solar cells: combining theories with practices. J Power Sour 402:82–90

140. Ishihara H, Chen WJ, Chen YC et al (2016) Photovoltaics: electrohydrodynamically assisted deposition of efficient perovskite photovoltaics (adv. mater. interfaces 9/2016). Adv Mater Interfaces 3(9):1500762

141. Remeika M, Ruiz Raga SR, Zhang SJ et al (2017) Transferrable optimization of spray-coated PbI$_2$ films for perovskite solar cell fabrication. J Mater Chem A 5(12):5709–5718

142. Mohamad D, Griffin J, Bracher C et al (2016) Spray-cast multilayer organometal perovskite solar cells fabricated in air. Adv Energy Mater 6:1600994

143. Sanjib D, Bin Y, Gong G et al (2015) High-performance flexible perovskite solar cells by using a combination of ultrasonic spray-coating and low thermal budget photonic curing. ACS Photon 2(6):680–686

144. Guo AZ, Chou LH, Yang SH et al (2020) Multi-channel pumped ultrasonic spray-coating for high-throughput and scalable mixed halide perovskite solar cells. Adv Mater Interfaces 8:2001509

145. Uličná S, Dou BJ, Kim DH et al (2018) Scalable deposition of high efficiency perovskite solar cells by spray-coating. ACS Appl Energy Mater 1(5):1853–1857. https://doi.org/10.1021/acsaem.8b00328

146. Green MA, Hishikawa Y, Dunlop ED et al (2017) Solar cell efficiency tables (version 51). Prog Photovolt Res Appl 26(3):12. https://doi.org/10.1002/PIP.287626

147. Hu Y, Chu YM, Wang QF et al (2019) Standardizing perovskite solar modules beyond cells. Joule 3(9):2076–2085. https://doi.org/10.1016/j.joule.2019.08.015

148. Li Z, Klein TR, Kim DH et al (2018) Scalable fabrication of perovskite solar cells. Nat Rev Mater 3:18017

149. Zhao XM, Liu TR, Burlingame QC et al (2022) Accelerated aging of all-inorganic, interface-stabilized perovskite solar cells. Science 377(6603):307–310

150. Gao LL, Chen L, Huang SY et al (2019) Series and parallel module design for large-area perovskite solar cells. ACS Appl Energy Mater 2(5):3851–3859

151. Wilkinson B, Chang NL, Green MA et al (2018) Scaling limits to large area perovskite solar cell efficiency. Prog Photovolt Res Appl 26(8):659–674

152. Kim DH, Whitaker JB, Li Z et al (2018) Outlook and challenges of perovskite solar cells toward terawatt-scale photovoltaic module technology. Joule 2(8):1437–1451

153. Hambsch M, Lin QQ, Armin A et al (2016) Efficient, monolithic large area organohalide perovskite solar cells. J Mater Chem A 4(36):13830–13836

154. Matteocci F, Cinà L, Di Giacomo FFD et al (2016) High efficiency photovoltaic module based on mesoscopic organometal halide perovskite. Prog Photovolt Res Appl 24(4):436–445

155. Werner J, Boyd CC, Moot T et al (2020) Learning from existing photovoltaic technologies to identify alternative perovskite module designs. Energy Environ Sci 13(10):3393–3403

156. Kato Y, Ono L, Lee MV et al (2015) Perovskite solar cells: silver iodide formation in methyl ammonium lead iodide perovskite solar cells with silver top electrodes. Adv Mater Interfaces 2:1500195

157. Jeong M, Choi IW, Yim K et al (2022) Large-area perovskite solar cells employing spiro-Naph hole transport material. Nat Photon 16(2):119–125

158. Bayer L, Ye XY, Lorenz P et al (2017) Studies on perovskite film ablation and scribing with ns-, ps- and fs-laser pulses. Appl Phys A 123(10):619. https://doi.org/10.1007/s00339-017-1234-5

159. Ernst M, Herterich J-P, Margenfeld C et al (2021) Multilayer blade-coating fabrication of methylammonium-free perovskite photovoltaic modules with 66 cm^2 active area. Sol RRL 6:2100535

160. Galagan Y (2018) Perovskite solar cells: toward industrial-scale methods. J Phys Chem Lett 9(15):4326–4335

161. Moon SJ, Yum JH, Löfgren L et al (2015) Laser-scribing patterning for the production of organometallic halide perovskite solar modules. IEEE J Photovolt 5(4):1087–1092. https://doi.org/10.1109/JPHOTOV.2015.2416913

162. Rong YG, Ming Y, Ji WX et al (2018) Toward industrial-scale production of perovskite solar cells: screen printing, slot-Die coating, and emerging techniques. J Phys Chem Lett 9(10):2707–2713

163. da Silva Filho JMC, Gonçalves AD, Marques FC et al (2021) A review on the development of metal grids for the upscaling of perovskite solar cells and modules. Sol RRL 6:2100865

164. Asghar MI, Zhang J, Wang H et al (2017) Device stability of perovskite solar cells—a review. Renew Sustain Energy Rev 77:131–146

165. Li NX, Niu XX, Chen Q et al (2020) Towards commercialization: The operational stability of perovskite solar cells. Chem Soc Rev 49(22):8235–8286

166. Wang D, Wright M, Elumalai NK et al (2016) Stability of perovskite solar cells. Sol Energy Mater Sol Cells 147:255–275. https://doi.org/10.1016/j.solmat.2015.12.025

167. Zhao Y, Zhou WK, Han ZY et al (2021) Effects of ion migration and improvement strategies for the operational stability of perovskite solar cells. Phys Chem Chem Phys 23(1):94–106. https://doi.org/10.1039/D0CP04418K/

168. Yang ZC, Liu ZH, Ahmadi V et al (2021) Recent progress on metal halide perovskite solar minimodules. Sol RRL 6(3):2100458. https://doi.org/10.1002/solr.202100458

169. Park NG, Zhu K (2020) Scalable fabrication and coating methods for perovskite solar cells and solar modules. Nat Rev Mater 5(5):333–350

170. Wu SH, Chen R, Zhang SS et al (2019) A chemically inert bismuth interlayer enhances long-term stability of inverted perovskite solar cells. Nat Commun 10(1):1161

171. Domanski K, Correa-Baena JP, Mine N et al (2016) Not all that glitters is gold: metal-migration-induced degradation in perovskite solar cells. ACS Nano 10(6):6306–6314

172. Zhang SSS, Liu ZZZH, Zhang WWJ et al (2020) Barrier designs in perovskite solar cells for long-term stability. Adv Energy Mater 10(35):2001610. https://doi.org/10.1002/aenm.202001610

173. Luo Q, Ma H, Hou QZ et al (2018) All-carbon-electrode-based endurable flexible perovskite solar cells. Adv Funct Mater 28(11):1706777. https://doi.org/10.1002/adfm.201706777

174. Zhou CH, Lin SY (2019) Carbon electrode-based perovskite solar cells: effect of bulk engineering and interface engineering on the

power conversion properties. Sol RRL 4(2):1900190. https://doi.org/10.1002/solr.201900190

175. Yuan JB, Rujisamphan N, Ma WL et al (2021) Perspective on the perovskite quantum dots for flexible photovoltaics. J Energy Chem 62:505–507. https://doi.org/10.1016/j.jechem.2021.04.024

176. Chen ZZ, Guo YW, Wertz E et al (2019) Merits and challenges of ruddlesden-popper soft halide perovskites in electro-optics and optoelectronics. Adv Mater 31(1):e1803514

Yixin Zhao is a professor at Shanghai Jiao Tong University. He graduated from Shanghai Jiao Tong University with B.S. and M.S. degrees in chemistry and received his Ph.D. degree from Case Western Reserve University, in 2010, followed by working as a postdoctoral fellow at Penn State University and National Renewable Energy Laboratory. His current research interests focus on perovskite solar cells and perovskite-based functional materials for solar energy conversion and environmental remediation application.

Yanfeng Miao received his Ph.D. degree at the Institute of Advanced Materials (IAM), Nanjing Tech University, in 2019, followed by working as a postdoctoral fellow at Shanghai Jiao Tong University. He is currently an assistant research fellow at Shanghai Jiao Tong University. His research interests focused on efficient and stable perovskite solar cells.